



High-redshift Galaxy Candidates at $z = 9$ – 10 as Revealed by JWST Observations of WHL0137-08

Larry D. Bradley¹ , Dan Coe^{1,2,3} , Gabriel Brammer^{4,5} , Lukas J. Furtak⁶ , Rebecca L. Larson^{7,35} , Vasily Kokorev⁸ , Felipe Andrade-Santos^{9,10} , Rachana Bhatawdekar¹¹ , Maruša Bradač^{12,13} , Tom Broadhurst^{14,15,16} , Adam Carnall¹⁷ , Christopher J. Conselice¹⁸ , Jose M. Diego¹⁹ , Brenda Frye²⁰ , Seiji Fujimoto^{4,5,21,36} , Tiger Y.-Y. Hsiao³ , Taylor A. Hutchison^{22,37} , Intae Jung¹ , Guillaume Mahler^{23,24} , Stephan McCandliss³ , Masamune Oguri^{25,26} , Marc Postman¹ , Keren Sharon²⁷ , M. Trenti^{28,29} , Eros Vanzella³⁰ , Brian Welch^{31,32,33} , Rogier A. Windhorst³⁴ , and Adi Zitrin⁶

¹ Space Telescope Science Institute (STScI), 3700 San Martin Drive, Baltimore, MD 21218, USA; lbradley@stsci.edu

² Association of Universities for Research in Astronomy (AURA) for the European Space Agency (ESA), STScI, Baltimore, MD, USA

³ Center for Astrophysical Sciences, Department of Physics and Astronomy, The Johns Hopkins University, 3400 N Charles St. Baltimore, MD 21218, USA

⁴ Cosmic Dawn Center (DAWN), Copenhagen, Denmark

⁵ Niels Bohr Institute, University of Copenhagen, Jagtvej 128, Copenhagen, Denmark

⁶ Physics Department, Ben-Gurion University of the Negev, P.O. Box 653, Be'er-Sheva 84105, Israel

⁷ The University of Texas at Austin, Department of Astronomy, Austin, TX, USA

⁸ Kapteyn Astronomical Institute, University of Groningen, P.O. Box 800, 9700AV Groningen, The Netherlands

⁹ Department of Liberal Arts and Sciences, Berklee College of Music, 7 Haviland Street, Boston, MA 02215, USA

¹⁰ Center for Astrophysics | Harvard & Smithsonian, 60 Garden Street, Cambridge, MA 02138, USA

¹¹ European Space Agency, ESA/ESTEC, Keplerlaan 1, 2201 AZ Noordwijk, The Netherlands

¹² University of Ljubljana, Department of Mathematics and Physics, Jadranska ulica 19, SI-1000 Ljubljana, Slovenia

¹³ Department of Physics and Astronomy, University of California Davis, 1 Shields Avenue, Davis, CA 95616, USA

¹⁴ Department of Theoretical Physics, University of the Basque Country UPV/EHU, Bilbao, Spain

¹⁵ Donostia International Physics Center (DIPC), 20018 Donostia, Spain

¹⁶ IKERBASQUE, Basque Foundation for Science, Bilbao, Spain

¹⁷ Institute for Astronomy, University of Edinburgh, Royal Observatory, Edinburgh EH9 3HJ, UK

¹⁸ Jodrell Bank Centre for Astrophysics, University of Manchester, Oxford Road, Manchester UK

¹⁹ Instituto de Física de Cantabria (CSIC-UC). Avda. Los Castros s/n. E-39005 Santander, Spain

²⁰ Department of Astronomy, Steward Observatory, University of Arizona, 933 North Cherry Avenue, Tucson, AZ 85721, USA

²¹ Department of Astronomy, The University of Texas at Austin, Austin, TX 78712, USA

²² Astrophysics Science Division, NASA Goddard Space Flight Center, 8800 Greenbelt Rd, Greenbelt, MD 20771, USA

²³ Institute for Computational Cosmology, Durham University, South Road, Durham DH1 3LE, UK

²⁴ Centre for Extragalactic Astronomy, Durham University, South Road, Durham DH1 3LE, UK

²⁵ Center for Frontier Science, Chiba University, 1-33 Yayoi-cho, Inage-ku, Chiba 263-8522, Japan

²⁶ Department of Physics, Graduate School of Science, Chiba University, 1-33 Yayoi-Cho, Inage-Ku, Chiba 263-8522, Japan

²⁷ Department of Astronomy, University of Michigan, 1085 S. University Ave, Ann Arbor, MI 48109, USA

²⁸ School of Physics, University of Melbourne, Parkville 3010, VIC, Australia

²⁹ ARC Centre of Excellence for All Sky Astrophysics in 3 Dimensions (ASTRO 3D), Australia

³⁰ INAF—OAS, Osservatorio di Astrofisica e Scienza dello Spazio di Bologna, via Gobetti 93/3, I-40129 Bologna, Italy

³¹ Department of Astronomy, University of Maryland, College Park, MD 20742, USA

³² Observational Cosmology Lab, NASA Goddard Space Flight Center, Greenbelt, MD 20771, USA

³³ Center for Research and Exploration in Space Science and Technology, NASA/GSFC, Greenbelt, MD 20771, USA

³⁴ School of Earth and Space Exploration, Arizona State University, Tempe, AZ 85287-1404, USA

Received 2022 October 4; revised 2023 August 1; accepted 2023 August 1; published 2023 September 12

Abstract

We report the discovery of four galaxy candidates observed 450–600 Myr after the Big Bang with photometric redshifts between $z \sim 8.3$ and 10.2 measured using James Webb Space Telescope (JWST) NIRCam imaging of the galaxy cluster WHL0137–08 observed in eight filters spanning 0.8 – $5.0 \mu\text{m}$, plus nine Hubble Space Telescope filters spanning 0.4 – $1.7 \mu\text{m}$. One candidate is gravitationally lensed with a magnification of $\mu \sim 8$, while the other three are located in a nearby NIRCam module with expected magnifications of $\mu \lesssim 1.1$. Using SED fitting, we estimate the stellar masses of these galaxies are typically in the range $\log M_*/M_\odot = 8.3$ – 8.7 . All appear young, with mass-weighted ages < 240 Myr, low dust content $A_V < 0.15$ mag, and specific star formation rates $\text{sSFR} \sim 0.25$ – 10 Gyr^{-1} for most. One $z \sim 9$ candidate is consistent with an age < 5 Myr and an $\text{sSFR} \sim 10 \text{ Gyr}^{-1}$, as inferred from a strong F444W excess, implying $[\text{O III}] + \text{H } \beta$ rest-frame equivalent width $\sim 2000 \text{ \AA}$, although an older $z \sim 10$ object is also allowed. Another $z \sim 9$ candidate is lensed into an arc $2''.4$ long with a magnification of $\mu \sim 8$. This arc is the most spatially resolved galaxy at $z \sim 9$ known to date, revealing structures ~ 30 pc across.

³⁵ NSF Graduate Fellow.

³⁶ Hubble Fellow.

³⁷ NASA Postdoctoral Fellow.



Original content from this work may be used under the terms of the [Creative Commons Attribution 4.0 licence](https://creativecommons.org/licenses/by/4.0/). Any further distribution of this work must maintain attribution to the author(s) and the title of the work, journal citation and DOI.

Follow-up spectroscopy of WHL0137–08 with JWST/NIRSpec will be useful to spectroscopically confirm these high-redshift galaxy candidates and to study their physical properties in more detail.

Unified Astronomy Thesaurus concepts: [High-redshift galaxies \(734\)](#); [Galaxy clusters \(584\)](#); [Strong gravitational lensing \(1643\)](#)

1. Introduction

The James Webb Space Telescope (JWST), with its 6.5 m aperture and infrared capabilities (Rigby et al. 2023), has opened a new window to study galaxies in the early Universe. In the first weeks of JWST science observation, a wealth of distant galaxy candidates (Naidu et al. 2022a; Castellano et al. 2022; Finkelstein et al. 2022; Adams et al. 2023; Atek et al. 2023; Donnan et al. 2023; Harikane et al. 2023) were reported from the JWST Early Release Observations (ERO; Pontoppidan et al. 2022), as well as the Cosmic Evolution Early Release Science (CEERS; Finkelstein et al. 2023) and Through the Looking GLASS (GLASS-JWST; Treu et al. 2022) Early Release Science (ERS) programs, that surpass the distance record set by the Hubble Space Telescope (HST) at $z = 11.1$ (Oesch et al. 2016). These independent studies have revealed an unexpectedly large abundance of bright galaxies ($M_{UV} \lesssim -21$; e.g., Naidu et al. 2022a; Finkelstein et al. 2022; Atek et al. 2023; Furtak et al. 2023) that could pose a challenge to our current models of galaxy formation (Naidu et al. 2022b; Ferrara et al. 2023; Harikane et al. 2023). Similarly, some $z \sim 7$ –11 candidates were reported to have surprisingly large stellar masses $M_* > 10^{10} M_\odot$ (Labbé et al. 2023) in apparent tension with Λ CDM (Boylan-Kolchin 2023; Lovell et al. 2023) unless these galaxies have lower masses (Endsley et al. 2023; Steinhardt et al. 2023) or incorrect redshifts.

Simulations suggest we should not have expected to find overly massive galaxies in early JWST observations, but rather that we have likely only discovered the youngest, most actively star-forming galaxies given imaging depths to date of AB mag ~ 29 (Mason et al. 2023). Analyses of these $z \sim 9$ –16 candidates observed in JWST imaging further reveal young stellar ages ~ 10 –100 Myr (Furtak et al. 2023; Whitler et al. 2023), younger than the median ages ~ 100 Myr measured at slightly lower redshifts $z \sim 7$ –9 (Endsley et al. 2023; Leethochawalit et al. 2023). Evidence that some of these galaxies are extremely young, < 10 Myr, $z \sim 7$ –9 is provided by very strong emission lines in NIRSpec spectroscopy (Carnall et al. 2023; Tacchella et al. 2023; Trussler et al. 2023), with flux excesses also clearly observed in photometry, especially when imaging is available in four NIRCcam long-wavelength filters F277W, F356W, F410M, and F444W.

Gravitational lensing by massive galaxy clusters can address these problems in some detail, as it provides magnified distant galaxies, boosting their luminosity and revealing small-scale structures that would otherwise be unobservable. Using these “cosmic telescopes,” surveys such as CLASH (Postman et al. 2012), the Hubble Frontier Fields (Lotz et al. 2017), and RELICS (Coe et al. 2019) have revealed hundreds of galaxy candidates in the reionization epoch. Using this technique, we have discovered highly magnified (Bradley et al. 2008, 2014; Zheng et al. 2012; Bouwens et al. 2014; Infante et al. 2015; Hoag et al. 2017; Salmon et al. 2018, 2020) and multiply imaged galaxies (Frye & Broadhurst 1998; Frye et al. 2008; Coe et al. 2013; Zitrin et al. 2014) at redshifts up to $z \sim 10.8$, many of which were the most distant known galaxy at the time of their discovery. Recent JWST observations of lensing

clusters have pushed this frontier even further, with many high-redshift candidates detected in ERO observations of the massive galaxy cluster SMACS0723 (Adams et al. 2023; Atek et al. 2023; Donnan et al. 2023; Harikane et al. 2023; Morishita & Stiavelli 2023) and the GLASS-JWST cluster Abell 2744 (Naidu et al. 2022a; Castellano et al. 2022; Donnan et al. 2023; Harikane et al. 2023; Leethochawalit et al. 2023), with photometric redshifts out to $z \sim 16$ (Atek et al. 2023).

Gravitationally lensed galaxies have allowed us to place strong constraints on the evolution of the galaxy ultraviolet luminosity function and the star formation rate density at $z > 8$ (Bouwens et al. 2014, 2017, 2022; Atek et al. 2015, 2018; Ishigaki et al. 2015; Laporte et al. 2015; Livermore et al. 2017; Bhatawdekar et al. 2019). Gravitational lensing has also provided us the ability to study small-scale structures and star clusters within high-redshift galaxies down to scales of a few parsecs (e.g., Meštrić et al. 2022; Vanzella et al. 2022; Welch et al. 2023).

The Reionization Lensing Cluster Survey (RELICS) HST Treasury Program (Coe et al. 2019) was designed to efficiently discover high-redshift galaxy candidates bright enough for follow-up observations with current and future observatories, including the Atacama Large Millimeter/submillimeter Array (ALMA) and JWST. By observing 41 strong lensing galaxy clusters with Hubble and Spitzer, RELICS discovered and studied over 300 high-redshift candidates in the first billion years (Salmon et al. 2020; Strait et al. 2021), including the brightest robust candidates known at $z \sim 6$, the Sunrise Arc, a $2''.5$ long arc at $z \sim 6$ (Salmon et al. 2020), and the most distant spatially resolved lensed arc, SPT0615-JD1, at $z \sim 10$ (Salmon et al. 2018). Remarkably, the RELICS survey also discovered the gravitationally lensed star WHL0137-LS, nicknamed Earendel, with a photometric redshift $z_{\text{phot}} = 6.2 \pm 0.1$ (Welch et al. 2022).

Earendel was discovered within the $z \sim 6$ Sunrise Arc (Welch et al. 2023) lensed by the massive galaxy cluster WHL J013719.8–082841 (hereafter WHL0137–08; R.A. = 01:37:25.0, decl. = $-08:27:23$, J2000), which is the focus of this paper. WHL0137–08 was discovered by Wen et al. (2012) based on photometric redshifts in SDSS-III DR8 (Aihara et al. 2011) and has a spectroscopic redshift of $z = 0.566$ based on two cluster members within $r_{500} = 0.82$ Mpc from its brightest cluster galaxy (Wen & Han 2015). The Planck SZ survey also identified this cluster (WHL-J24.3324-8.477) as the 31st most massive in the Planck PSZ2 catalog with $M_{500} = (8.9 \pm 0.7) \times 10^{14} M_\odot$ (Planck Collaboration et al. 2016).

In this paper, we present high-redshift candidates at $z \sim 8.3$ –10.2 discovered in JWST NIRCcam imaging of WHL0137–08, obtained primarily to study Earendel (Welch et al. 2022) and the Sunrise Arc in more detail. Our sample includes both a strongly lensed galaxy candidate discovered behind the cluster and three candidates in the nearby NIRCcam module, centered $\sim 2''.9$ from the cluster center, with weak magnifications of $\mu \leq 1.1$. We use the AB magnitude system, $m_{\text{AB}} = 31.4 - 2.5 \log(f_\nu / \text{nJy})$ (Oke 1974; Oke & Gunn 1983). Where needed, we adopt a Planck 2018 flat Λ CDM cosmology (Planck Collaboration et al. 2020) with $H_0 = 67.7 \text{ km s}^{-1} \text{ Mpc}^{-1}$,

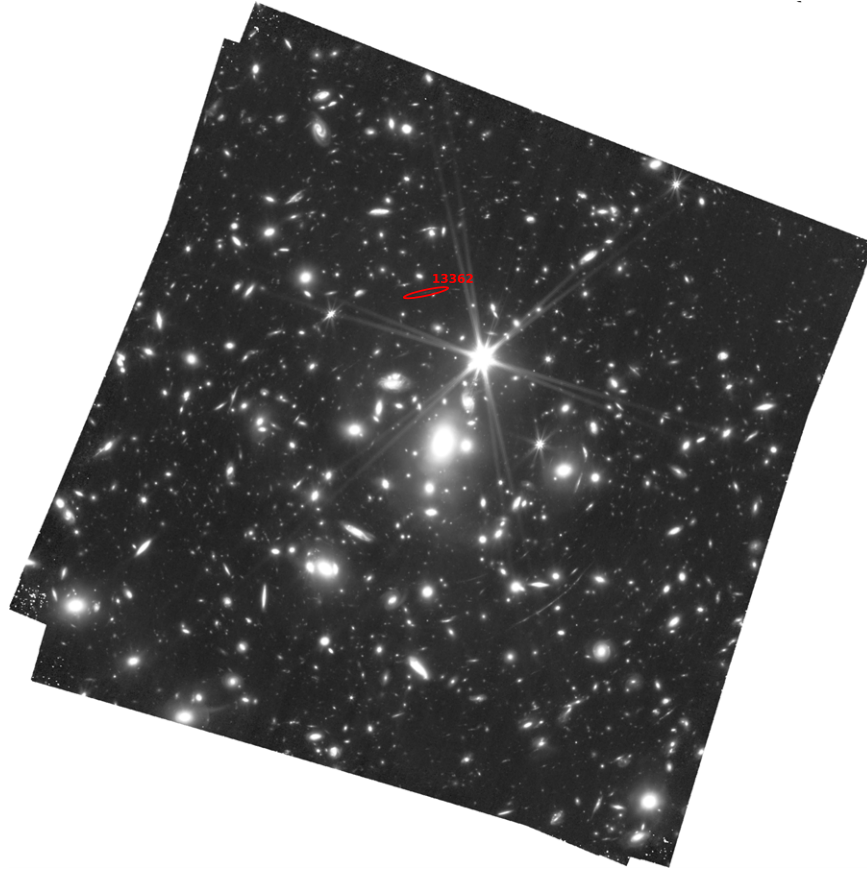


Figure 1. JWST NIRCам detection image, comprised of a weighted sum of all NIRCам LW images (F277W, F356W, F410M, F444W), of the WHL0137–08 cluster field. The field of view is $\sim 2' 3 \times 2' 3$, and the image is shown with north up and east left. The location of the strongly lensed $z \sim 9$ high-redshift candidate in the WHL0137–08 cluster field is indicated with a red ellipse. The locations of the other high-redshift candidates are shown in Figure 2.

$\Omega_m = 0.31$, and $\Omega_\Lambda = 0.69$, for which the Universe is 13.8 billion years old and $1'' \sim 4.6$ kpc at $z = 9$.

All of the JWST and HST data of WHL0137–08 are public. Reduced images, catalogs, lens models, and analysis code are available via our website.³⁸

2. Observations

2.1. JWST Data

We obtained JWST NIRCам imaging of WHL0137–08 (GO 2282, PI Coe) in 2022 July and 2023 January as part of a program to further study Earendel and the Sunrise Arc. The first epoch of NIRCам observations cover eight filters (F090W, F115W, F150W, F200W, F277W, F356W, F410M, and F444W) spanning $0.8\text{--}5.0\ \mu\text{m}$ with 2104 s of exposure time in each filter. The NIRCам imaging was obtained over two $2' 26 \times 2' 26$ fields separated by $40'' 5$, covering $10.2\ \text{arcmin}^2$ in total. For the first epoch, the WHL0137–08 cluster was centered on NIRCам module B while NIRCам module A obtained observations on a nearby field centered $\sim 2' 9$ northwest of the cluster center. For the second epoch, the NIRCам observations cover four filters (F090W, F115W, F277W, and F356W) with 2104 s of exposure time in each filter. The observations for the second epoch were obtained 185° from the first epoch. The cluster was again centered on NIRCам module B, while NIRCам module A obtained observations on another nearby field southeast of the cluster

center. Because this second parallel field has imaging only in four filters, we do not use it in this analysis.

Each exposure uses the SHALLOW4 readout pattern with ten groups and one integration. We use the INTRAMODULE-BOX dither pattern with four dithers to fill the $5''$ gaps in the short-wavelength detectors and to maximize the area with full exposure time. The dither pattern also mitigates the effects of bad pixels and image artifacts, and it improves the spatial resolution of the resampled/drizzled images.

2.2. HST Data

The RELICS HST Treasury program (GO 14096; Coe et al. 2019) obtained the first HST imaging of the galaxy cluster WHL0137–08 in 2016 with three orbits of ACS (F435W, F606W, and F814W) and two orbits of WFC3/IR (F105W, F125W, F140W, and F160W) data spanning $0.4\text{--}1.7\ \mu\text{m}$. Two follow-up HST imaging programs (GO 15842 and GO 16668; PI: Coe) have thus far obtained an additional five orbits of HST ACS imaging in F814W, two orbits in F475W, and four orbits with WFC3/IR in F110W. Two more orbits of WFC3/IR F110W data are yet to be obtained from the Earendel monitoring program (GO 16668). The HST data cover only the cluster field.

In total, the JWST and HST observations of WHL0137–08 include imaging in 17 filters spanning $0.4\text{--}5.0\ \mu\text{m}$. We show color images of the JWST data in Figures 1 and 2. The observations are summarized in Table 1.

³⁸ <https://cosmic-spring.github.io>

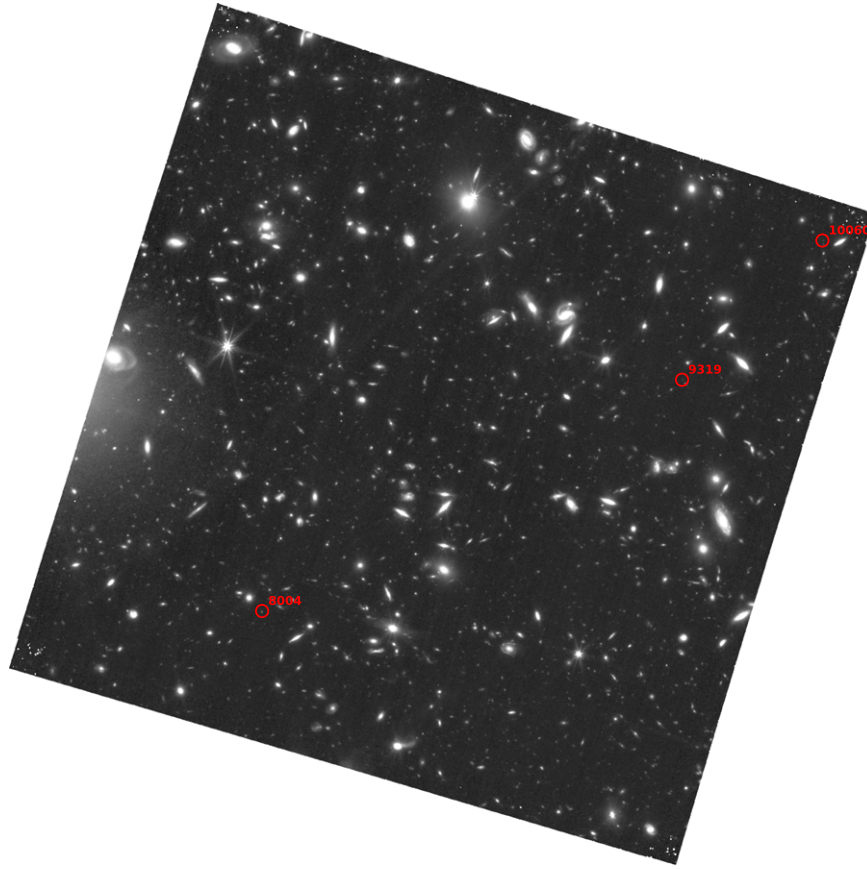


Figure 2. JWST NIRCам detection image, comprised of a weighted sum of all NIRCам LW images (F277W, F356W, F410M, and F444W), of the nearby field (NIRCам A module), centered $\sim 2''.9$ from the WHL0137–08 cluster center. The field of view is $\sim 2''.3 \times 2''.3$ and the image is shown with north up and east left. The locations of the high-redshift candidates are indicated with red circles. The location of the lensed high-redshift candidate is shown in Figure 1.

3. Methods

3.1. Data Reduction

We retrieved the pipeline-calibrated HST data and the JWST level-2 imaging products and processed them using the GRIZLI³⁹ (version 1.8.12) reduction pipeline (Brammer et al. 2022). The calibrated HST optical and near-infrared data were obtained from Complete Hubble Archive for Galaxy Evolution (CHArGE; Kokorev et al. 2022). The GRIZLI image reduction process is described in Valentino et al. (2023). The JWST data were processed with version 1.9.6 of the calibration pipeline with the latest CRDS context `jwst_1093.pmap`, which includes the most recent photometric calibrations based on in-flight data.

For the JWST data, the GRIZLI reduction pipeline applies a correction to reduce the effect of $1/f$ noise and masks “snowballs”⁴⁰ that are caused by large cosmic ray impacts to the NIRCам detectors. The GRIZLI pipeline also includes a correction for faint, diffuse stray-light features, called “wisps,”⁴¹ that are present at the same detector locations in NIRCам images. These stray-light features are most prominent in the NIRCам A3, B3, and B4 detectors in the F150W and F200W data. A “wisp” template was subtracted from each of these detectors for both the F150W and F200W data.

The GRIZLI pipeline aligns the HST and JWST data to a common world coordinate system registered to the GAIA DR3 catalogs (Gaia Collaboration et al. 2021). The fully calibrated images in each filter were combined and drizzled to a common pixel grid using ASTRODRIZZLE (Koekemoer et al. 2003; Hoffmann et al. 2021). The HST and JWST NIRCам long-wavelength (LW) filters (F277W, F356W, F410M, and F444W) were drizzled to a grid of $0''.04$ per pixel, while the JWST short-wavelength NIRCам filters (F090W, F115W, F150W, and F200W) were drizzled to a grid of $0''.02$ per pixel.

These GRIZLI-reduced images are available publicly, alongside images and catalogs from other JWST programs with public data.⁴²

3.2. Photometric Catalogs

To produce the photometric catalogs, the NIRCам SW images were first rebinned to a pixel scale of $0''.04$ per pixel, placing the images for all 17 filters on the same pixel grid. Sources were then identified in a detection image comprised of a weighted sum of the F277W, F356W, and F444W NIRCам LW images using PHOTUTILS (Bradley 2023) image-segmentation tools. Visual inspection of the segmentation image revealed a $2''.4$ long lensed arc that had been segmented into five separate components. Therefore, we combined the separate arc segments into a single source before performing photometry.

Source fluxes were measured with PHOTUTILS in flexible elliptical Kron apertures with a scale factor of 1.5. The size of

³⁹ <https://github.com/gbrammer/grizli>

⁴⁰ <https://jwst-docs.stsci.edu/data-artifacts-and-features/snowballs-artifact>

⁴¹ <https://jwst-docs.stsci.edu/jwst-near-infrared-camera/nircam-features-and-caveats/nircam-claws-and-wisps>

⁴² https://jwst-grizli.s3.amazonaws.com/sunrise-new/sunrise-v2_index.html

Table 1
HST and JWST Exposure Times and Depths

Camera	Filter	Wavelength (μm)	Cluster Field			Parallel Field		
			Exposure Time (s)	$m_{\text{lim}}^{\text{a}}$ (nJy)	$f_{\text{lim}}^{\text{b}}$ (AB)	Exposure Time (s)	$m_{\text{lim}}^{\text{a}}$ (nJy)	$f_{\text{lim}}^{\text{b}}$ (AB)
HST ACS/WFC	F435W	0.37–0.47	2072	27.7	29.5
HST ACS/WFC	F475W	0.4–0.55	3988	28.5	14.9
HST ACS/WFC	F606W	0.47–0.7	2072	28.4	16.5
HST ACS/WFC	F814W	0.7–0.95	13326	28.8	10.5
HST WFC3/IR	F105W	0.9–1.2	1411	27.9	25.4
HST WFC3/IR	F110W	0.9–1.4	10047	29.4	6.17
HST WFC3/IR	F125W	1.1–1.4	711	27.3	42.8
HST WFC3/IR	F140W	1.2–1.6	711	27.5	37.0
HST WFC3/IR	F160W	1.4–1.7	1961	27.9	25.5
JWST NIRCcam	F090W	0.8–1.0	4208	28.6	13.3	2104	28.4	16.0
JWST NIRCcam	F115W	1.0–1.3	4208	28.6	12.6	2104	28.4	15.5
JWST NIRCcam	F150W	1.3–1.7	2104	28.5	14.1	2104	28.6	13.2
JWST NIRCcam	F200W	1.7–2.2	2104	28.7	11.9	2104	28.7	11.7
JWST NIRCcam	F277W	2.4–3.1	4208	29.5	5.6	2104	29.3	6.7
JWST NIRCcam	F356W	3.1–4.0	4208	29.7	5.0	2104	29.4	6.1
JWST NIRCcam	F410M	3.8–4.3	2104	28.7	11.6	2104	28.8	11.2
JWST NIRCcam	F444W	3.8–5.0	2104	29.1	8.1	2104	29.1	8.1

Notes.

^a 5σ limiting AB magnitude in a $r = 0''.1$ circular aperture.

^b 5σ limiting flux in a $r = 0''.1$ circular aperture.

the elliptical Kron aperture is calculated for each source by multiplying the Kron scale factor by the Kron radius, which is calculated independently for each source using the first-order moment of its flux distribution. It has been shown that measuring colors in small elliptical apertures accurately recovers the colors of distant galaxies (Finkelstein et al. 2022, 2023). We then performed a second run of PHOTUTILS on the detection image using Kron apertures with a scale factor of 2.5. An aperture correction to the total flux for the small apertures was estimated as the ratio between the flux in the larger aperture and that in the smaller aperture for each source. We then applied this aperture correction to the fluxes and uncertainties for all filters.

3.3. Photometric Redshifts

We derive initial photometric redshifts using EAZY (Brammer et al. 2008), which fits the observed photometry of each galaxy using a set of templates added in a non-negative linear combination. We use the photometry measured in elliptical Kron apertures with a scale factor of 1.5. Both JWST and HST photometry are included in the photometric redshift calculations for the WHL0137–08 cluster field, while only JWST photometry is used for the Module A field. The photometric redshifts were calculated using a template set comprised of the 12 “tweak_fspc_QSF_12_v3” templates derived from the Flexible Stellar Population Synthesis (FSPS) library (Conroy et al. 2009; Conroy & Gunn 2010; Conroy et al. 2010), which include a range of galaxy types (e.g., star-forming, quiescent, and dusty) and realistic star formation histories (e.g., bursty, slowly rising, and slowly falling). To these FSPS templates, we add six templates from Larson et al. (2022) that span bluer colors than the fiducial FSPS templates. These additional templates were found to provide better photometric-redshift accuracies for bluer galaxies at $z > 9$ (Larson et al. 2022). We allow the redshifts to span from $0.1 < z < 20$, in

steps of 0.01. Because we are just beginning to explore galaxies at these epochs, the high-redshift luminosity function, especially at the bright end, is not well-known at $z \gtrsim 9$. Therefore, we adopt a flat luminosity prior, similar to recent similar to recent JWST high-redshift studies (e.g., Finkelstein et al. 2022, 2023; Adams et al. 2023), to prevent bias against the selection of bright high-redshift galaxies.

3.4. High-redshift Candidate Selection

We select our initial sample of high-redshift candidate galaxies using a combination of criteria using both signal-to-noise (S/N) and photometric redshift measurements. Measuring photometric redshifts using SED fitting is a well-established method for selecting high-redshift galaxy candidates that simultaneously uses the photometry in all bands (e.g., Bradley et al. 2014; Salmon et al. 2020; Naidu et al. 2022c; Finkelstein et al. 2022, 2023; Adams et al. 2023; Donnan et al. 2023). The photometric S/N criteria are used to both ensure nondetections in filters blueward of $\text{Ly}\alpha$ and to ensure robust photometric detections in multiple filters redward of the $\text{Ly}\alpha$ break, which minimizes spurious noise detections. We also visually inspect each candidate galaxy in each filter image and its best-fit SED to remove detector artifacts and other spurious sources such as diffraction spikes, misidentified parts of larger galaxies, and spurious noise close to the detector edge.

We use criteria similar to those of Finkelstein et al. (2023) to select our initial sample of high-redshift candidates while minimizing contamination from low-redshift interlopers:

1. An S/N of < 1.5 to ensure nondetections blueward of $\text{Ly}\alpha$ in all of the following filters: F435W, F475W, F606W, F814W, and F090W.
2. An S/N of > 5.5 in at least two the following filters: F115W, F150W, F200W, F277W, F356W, and F444W, to reduce spurious sources.

3. Best-fit photometric redshift measured by EAZY of $z_{\text{best}} \geq 8.5$
4. Integral of the EAZY posterior redshift probability ($P(z)$) at $z > 8$ of $\int P(z > 8) dz > 0.8$
5. χ^2 of the best-fit EAZY spectral energy distribution (SED) of $\chi^2 < 30$

We also require additional nondetections as a function of the redshift selection window as follows. For the $9.7 \leq z < 13$ sample, we require the F115W S/N < 1.5 . For the $z \geq 13$ sample, we require the F115W and F150W S/N < 1.5 . These filters are bluer than Ly α at these corresponding redshifts.

Additionally, we ran EAZY restricting the maximum redshift to $z < 7$. We then calculate the difference of the best-fit χ^2 for these “low-redshift” solutions and the best-fit χ^2 for the high-redshift solutions. For our high-redshift sample, we require a conservative $\Delta\chi^2 > 9$, ruling out the low-redshift model at $\geq 3\sigma$ significance (Harikane et al. 2023).

As a further check, we also calculated photometric redshifts using EAZY with the recently added SFHZ templates. These templates have redshift-dependent star formation histories (SFH) that disfavor star formation starting earlier than the age of the Universe at a given epoch. We excluded candidates from our high-redshift sample where these templates prefer a low-redshift ($z_{\text{best}} < 8.5$) solution.

4. Results and Discussion

4.1. High-redshift Sample

Our final sample consists of four high-redshift galaxy candidates. One of the candidates lies in the WHL0137–08 cluster field, while the remaining three are located in the nearby parallel field. As measured by EAZY, three of the candidates are at $8.5 \leq z < 9.7$, while the remaining candidate was identified in the $9.7 \leq z < 13$ selection.

The measured (uncorrected for magnification) JWST photometry of our high-redshift candidates is presented in Table 2. For the lensed high-redshift candidate in the cluster field, we also present its measured (uncorrected for magnification) HST photometry in Table 3. In Figures 3–4, we present $3'' \times 3''$ cutout images, the best-fit SEDs, and the posterior redshift distributions, $P(z)$, for each candidate. The posterior redshift distributions include plots for EAZY (for both the FSPS+ (Larson et al. 2022) and SFHZ template sets), BAGPIPES, and BEAGLE. We plot in Figures 3–4 the BAGPIPES best-fit high-redshift ($z \geq 7$) SED along with the best-fit low-redshift SED constrained with redshift $z < 7$.

We estimate the amplitude of the Ly α break in these candidates as 2.8, > 1.5 , > 1.8 , and > 1.5 magnitudes, which are significant breaks (factors of 3.5 – 13 in flux ratios). The upper limits were calculated using the measured flux uncertainty for the nondetection blueward of the break. Our measured break colors are larger than the break amplitude of 0.5 mag used to select $9 < z < 11$ high-redshift candidates in Atek et al. (2023), comparable to the 1.7 mag used to select $9 < z < 11.5$ candidates in Castellano et al. (2022), and consistent with the 1.5 ($z \sim 8$ selection) and 1.4 ($z \sim 10$ selection) break color criterion in Bouwens et al. (2023), who all used color–color selection criteria to select their high-redshift candidates.

4.2. Magnifications

To estimate source magnifications, we use the lens models constructed to analyze Earendel and the Sunrise Arc published in Welch et al. (2022) and which were made publicly available.⁴³ These models were generated using four independent lens modeling software packages: Light-Traces-Mass (LTM; Broadhurst et al. 2005; Zitrin et al. 2009, 2015), Glafic (Oguri 2010), WSLAP+ Diego et al. (2005, 2007), and Lenstool (Jullo et al. 2007; Jullo & Kneib 2009). Due to a lack of multiply imaged sources in this cluster, the slope of the lensing potential in these models varies by a factor of six, which adds considerable uncertainty to our magnification estimates. For further details about each model, please see Welch et al. (2022). The ratio of the source-plane area at $z = 9$ of the lensed cluster field to the nearby parallel field ranges from 0.24 to 0.85 (ratios of 0.24, 0.29, 0.68, and 0.85 for the four models). The large range is reflective of the uncertainty in the slope of the lensing potential.

One candidate in our sample is strongly lensed by the WHL0137–08 galaxy cluster, while the other three candidates, located in the nearby NIRCам module, are expected to have only weak magnifications of $\mu \leq 1.1$. The lensed candidate is WHL0137–ID13362 with a $z_{\text{phot}} \sim 9$. At this redshift, our lens models yield a magnification in the range from $\mu = 2.4$ to 20.2, with an arithmetic mean value of $\mu = 7.9$. The mean magnification for this candidate is quoted in Tables 3, 4, and 5.

4.3. Galaxy Sizes

We measure the half-light radius of the three unlensed candidates in the sample from the deeper detection image using the SourceCatalog class in PHOTUTILS. The half-light radius r_h is calculated relative to the “total” flux measured in elliptical Kron apertures with a Kron factor of 2.5. The derived sizes for WHL0137–ID8004, WHL0137–ID9319, and WHL0137–ID10060 are 3.3, 4.0, and 3.3 pixels ($0''.13$, $0''.16$, and $0''.13$), respectively. Therefore, all three sources are spatially resolved, being larger than the NIRCам F444W PSF full width at half maximum of $0''.145$ ($0''.0725$ radius). The lensed source, WHL0137–ID13362, is also spatially resolved, stretched into a $2''.4$ long arc by the effects of gravitational lensing. The morphology of the arc is discussed in more detail in Section 4.6.

Assuming the estimated BAGPIPES photometric redshifts (see Table 4) of the three unlensed sources, they have physical sizes of 0.60, 0.67, and 0.61 kpc, respectively. These sizes are comparable to the galaxy sizes found in the GLASS-JWST survey ranging from 0.17 to 2.01 kpc in F444W (Yang et al. 2022) and the CEERS survey, with sizes ranging from 0.05 to 1.1 kpc in F200W (Finkelstein et al. 2023).

4.4. Spectral Energy Distribution (SED) Fitting

4.4.1. BAGPIPES

For each galaxy in our high-redshift sample, we estimate its physical properties using SED fitting. We performed SED fitting using the Bayesian Analysis of Galaxies for Physical Inference and Parameter Estimation (BAGPIPES; Carnall et al. 2018) Python package and the Bayesian Analysis of Galaxy SEDs (BEAGLE; Chevallard & Charlot 2016) tool with redshift as a free parameter.

⁴³ https://relics.stsci.edu/lens_models/outgoing/whl0137-08/

Table 2
JWST Photometry for the Complete Sample of High-redshift Candidates

Object ID	R.A.	Decl.	F090W (nJy)	F115W (nJy)	F150W (nJy)	F200W (nJy)	F277W (nJy)	F356W (nJy)	F410M (nJy)	F444W (nJy)
WHL0137-08004	24.34989786	−8.41981970	-1.1 ± 6.1	15.8 ± 6.4	77.9 ± 5.7	86.0 ± 4.8	81.7 ± 3.7	115.3 ± 3.6	137.8 ± 6.4	249.3 ± 5.5
WHL0137-09319	24.32694954	−8.40731680	-4.0 ± 8.9	-19.9 ± 9.1	35.4 ± 7.7	40.6 ± 6.5	33.7 ± 4.6	38.2 ± 4.3	45.5 ± 7.7	42.8 ± 6.6
WHL0137-10060	24.31928158	−8.39978978	-16.3 ± 7.1	18.7 ± 7.2	38.8 ± 6.3	31.6 ± 5.2	27.1 ± 3.6	30.9 ± 3.3	33.7 ± 6.1	28.4 ± 5.2
WHL0137-13362 ^a	24.35501927	−8.44791625	-16.0 ± 11.3	42.5 ± 11.8	164.0 ± 12.9	125.1 ± 10.7	98.6 ± 5.9	98.5 ± 5.6	113.7 ± 14.4	165.9 ± 11.6

Notes. Observed fluxes, uncorrected for magnification. $m_{\text{AB}} = 31.4 - 2.5 \log(f_{\nu}/\text{nJy})$.

^a Lensed candidate with a magnification of $\mu = 8_{-6}^{+12}$. Other candidates (located in the nearby field) are estimated to have magnifications of $\mu \leq 1.1$.

Table 3
HST Photometry of the Lensed High-redshift Candidate

Object ID	F105W (nJy)	F110W (nJy)	F125W (nJy)	F140W (nJy)	F160W (nJy)	F435W (nJy)	F475W (nJy)	F606W (nJy)	F814W (nJy)	μ
WHL0137- 13362	83.7 ± 46.3	42.4 ± 9.6	70.7 ± 81.8	21.5 ± 68.8	28.5 ± 47.7	-36.7 ± 39.2	12.5 ± 17.7	-5.3 ± 22.8	1.7 ± 13.1	8_{-6}^{+12}

Note.

^a Observed fluxes, uncorrected for magnification. $m_{AB} = 31.4 - 2.5 \log(f_\nu/\text{nJy})$.

BAGPIPES generates model galaxy spectra over the multi-dimensional space of physical parameters and fits these to the photometric data using the MULTINEST nested sampling algorithm (Feroz & Hobson 2008; Feroz et al. 2009; Feroz & Skilling 2013). BAGPIPES uses the stellar population synthesis models from the 2016 version of the BC03 (Bruzual & Charlot 2003) models. These models were generated using a Kroupa (2002) initial mass function (IMF) and include nebular line and continuum emission based on CLOUDY (Ferland et al. 2013), with the logarithm of ionization parameter ($\log U$) allowed to vary between -4 and -2 . We perform our SED fitting using a delayed exponentially declining SFH where the star formation rate (SFR) is of the form $\text{SFR}(t) \propto t \exp(-t/\tau)$. Models assuming a constant star formation rate yield younger ages and higher sSFRs, as discussed below in Section 4.5.

For SED fits constrained to be at low redshift ($z < 7$), we assume a Calzetti law (Calzetti et al. 2000) for dust attenuation. For SED fits constrained to be at high redshift ($z > 7$), we assume a Small Magellanic Cloud (SMC) dust law (Salim et al. 2018). For both cases, we also include a second component to the dust model that includes birth-cloud dust attenuation that is a factor of two larger around H II regions as in the general ISM within the galaxy’s first 10 Myr. We allow dust extinction to range from $A_V = 0$ –5 magnitudes, and we vary metallicity in logarithmic space from $\log Z/Z_\odot = 0.005$ –5. Formation ages vary from 1 Myr to the age of the Universe.

4.4.2. BEAGLE

We also perform SED fitting on each candidate galaxy using the BEAGLE tool (Chevallard & Charlot 2016) with a simplified version of the configuration, fit parameters, and parameter space used in Atek et al. (2023) and Furtak et al. (2023). BEAGLE uses SED templates by Gutkin et al. (2016), which also combine the 2016 version of the BC03 stellar population synthesis models with CLOUDY to account for nebular emission. The templates include ionization parameters varying from -4 to -1 . These templates all assume a Chabrier (2003) IMF and model the intergalactic attenuation using the Inoue et al. (2014) attenuation curves. As with BAGPIPES, we assume a delayed exponential SFH, but with the possibility of an ongoing starburst over the last 10 Myr. This allows for maximum flexibility of the SFH to be either rising or declining with a maximum at $t = \tau$. We account for dust attenuation by assuming an SMC-like dust attenuation law (Pei 1992), which has been found to fit high-redshift galaxies best at low metallicities (Capak et al. 2015; Reddy et al. 2015, 2018; Shivaee et al. 2020). Due to the relatively large number of free parameters, we fix the metallicity to $Z = 0.1 Z_\odot$, while the stellar mass, current SFR, maximal stellar age, and dust attenuation are allowed to vary freely in the ranges $\log(M_*/M_\odot) \in [6, 11]$, $\log(\psi/M_\odot \text{ yr}^{-1}) \in [-4, 4]$, $\log(t_{\text{age}}/\text{yr}) \in [6, t_{\text{Universe}}]$, and $A_V \in [0, 3]$, respectively.

4.5. Physical Properties

The physical properties derived for our candidate high-redshift galaxies using BAGPIPES and BEAGLE are presented in Tables 4 and 5, respectively. The BAGPIPES physical parameter results are quoted for high-redshift solutions restricted to $z > 7$. For WHL0137–ID13362, we divide by its mean magnification (see Section 4.2) to calculate intrinsic stellar mass and SFR.

We estimate intrinsic stellar masses of $\log M_*/M_\odot \sim 8.3$ –8.7 for all galaxies with BAGPIPES and all but one with BEAGLE. The BAGPIPES SFRs range from ~ 1.2 to $4.5 M_\odot \text{ yr}^{-1}$, with specific star formation rates (sSFRs) of $\sim 1 \text{ Gyr}^{-1}$ (0.8 – 1.0 Gyr^{-1}). The BEAGLE SFRs range from ~ 0.1 to $5.4 M_\odot \text{ yr}^{-1}$, with sSFRs of 0.01 – 10 Gyr^{-1} . We note that BAGPIPES considers the most recent 100 Myr of star formation, while BEAGLE considers the most recent 10 Myr (sSFR results capped at 100 Gyr^{-1}).

In most cases, the SED fitting reveals relatively young ages of $< 132 \text{ Myr}$. The exception is the BEAGLE fit for WHL0137–ID08004 (discussed below), which has an age of 236 Myr. Median age estimates from BAGPIPES are typically $\sim 76 \text{ Myr}$, while BEAGLE median ages are typically younger ($\sim 34 \text{ Myr}$). Switching BAGPIPES to a constant star formation history (CSFH) also results in younger median ages typically $\sim 22 \text{ Myr}$.

For all candidates, we also find low dust content with $A_V < 0.15$, as expected due to the relatively blue rest-frame UV slopes in our sample of $\beta = -1.5$ to -2.6 (see Table 5).

The BEAGLE SED fits of WHL0137–ID08004 have the largest stellar mass, with $\log M_*/M_\odot = 10.19_{-0.04}^{+0.05}$, coupled with the lowest star formation rate, $0.1_{-0.1}^{+0.4} M_\odot \text{ yr}^{-1}$. This is a result of BEAGLE fitting the red $F410M - F444W = 0.6$ color as a Balmer break (see Figure 3; top), with an older mass-weighted age of $236_{-46}^{+44} \text{ Myr}$. On the other hand, BAGPIPES fits this galaxy as an extremely young (2_{-1}^{+1} Myr) galaxy with a high sSFR rate of $\sim 10 \text{ Gyr}^{-1}$ and strong inferred $[\text{O III}] + \text{H} \beta$ emission (rest-frame equivalent width of $\sim 2000 \text{ \AA}$). The BAGPIPES fit yields a more typical mass of $\log M_*/M_\odot = 8.39_{-0.07}^{+0.04}$.

The lensed galaxy WHL0137–ID13362 also has a red $F410M - F444W$ color of 0.4. For this candidate, both BAGPIPES and BEAGLE fit this galaxy with an SED template containing strong $[\text{O III}] + \text{H} \beta$ optical emission lines. BEAGLE gives a young age of 34 Myr, while BAGPIPES yields a slightly older age of 132 Myr.

4.5.1. SED Fitting Limitations

It is important to note that these physical property results rely on SED fitting to the broadband photometry, which is primarily in the rest-frame UV of these candidate high-redshift galaxies. This rest-frame wavelength regime is not ideally suited to investigate galaxy parameters, because it primarily probes very massive and short-lived stars in a galaxy, which may not

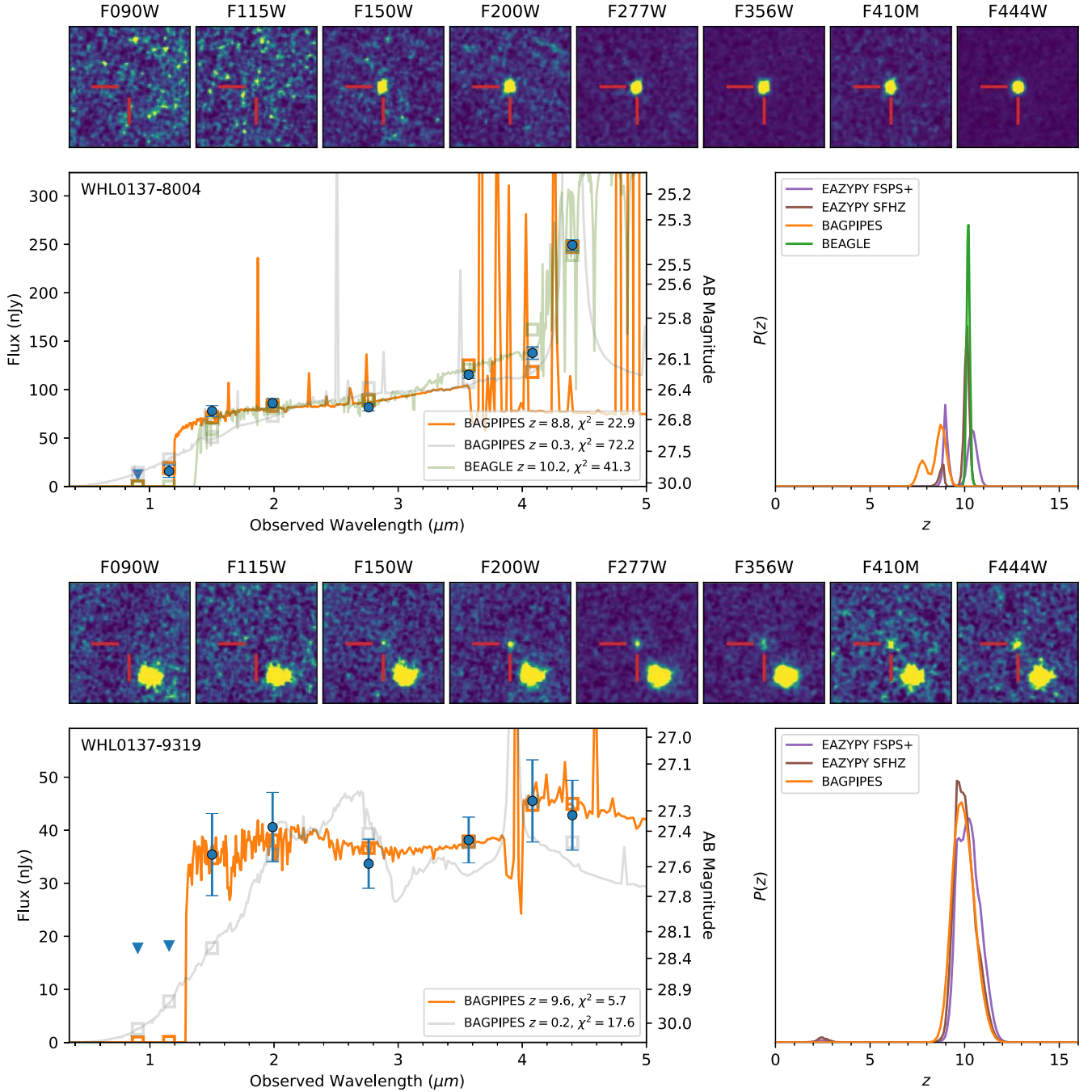


Figure 3. Cutout images, best-fit spectral energy distributions (SEDs), and posterior redshift distributions for the high-redshift galaxy candidates WHL0137-ID08004 and WHL0137-ID09319. Top panels: $3'' \times 3''$ JWST cutout images spanning $0.9\text{--}4.5\ \mu\text{m}$ centered on each candidate. Bottom left panels: Source photometry is shown as blue data points or triangle upper limits. Nondetections are plotted as upper limits at the 1σ level. The best-fit BAGPIPES spectral energy distribution (SED) model at high redshift ($z \geq 7$) is shown in orange, with squares indicating the expected photometry in a given band. The best-fit BAGPIPES SED for a low-redshift ($z < 7$) solution is shown in gray. For WHL0137-ID08004, we also show the best-fit BEAGLE SED model (see Section 4.5) in green. Bottom right panels: Posterior probability distributions $P(z)$ for the source photometric redshift derived using EAZYPY (using both the FSPS+ (Larson et al. 2022) and SFHZ template sets), BAGPIPES, and BEAGLE.

compose the bulk of its stellar mass. Because of limited rest-frame optical photometry, we expect SED fitting to underestimate the stellar masses. In particular, Furtak et al. (2021) showed that SED fitting to only UV photometry can underestimate stellar masses by up to 0.6 dex. Likewise, fitting primarily to rest-frame UV photometry can lead to some degeneracies between the stellar mass, SFR, and age (Furtak et al. 2023).

While the SED fitting results of BAGPIPES and BEAGLE are relatively consistent, they differ significantly for WHL0137-

ID8004, leading to completely different interpretations. As discussed above, BAGPIPES fits this galaxy with very strong [O III]+H β optical emission lines, while BEAGLE fits this galaxy with a strong Balmer break. These fitting differences result in highly uncertain physical properties for this galaxy, with the stellar mass differing by 1.4 dex, the SFR differing by $2.4\ M_{\odot}\ \text{yr}^{-1}$, and the mass-weighted age differing by 234 Myr (either extremely young or relatively old).

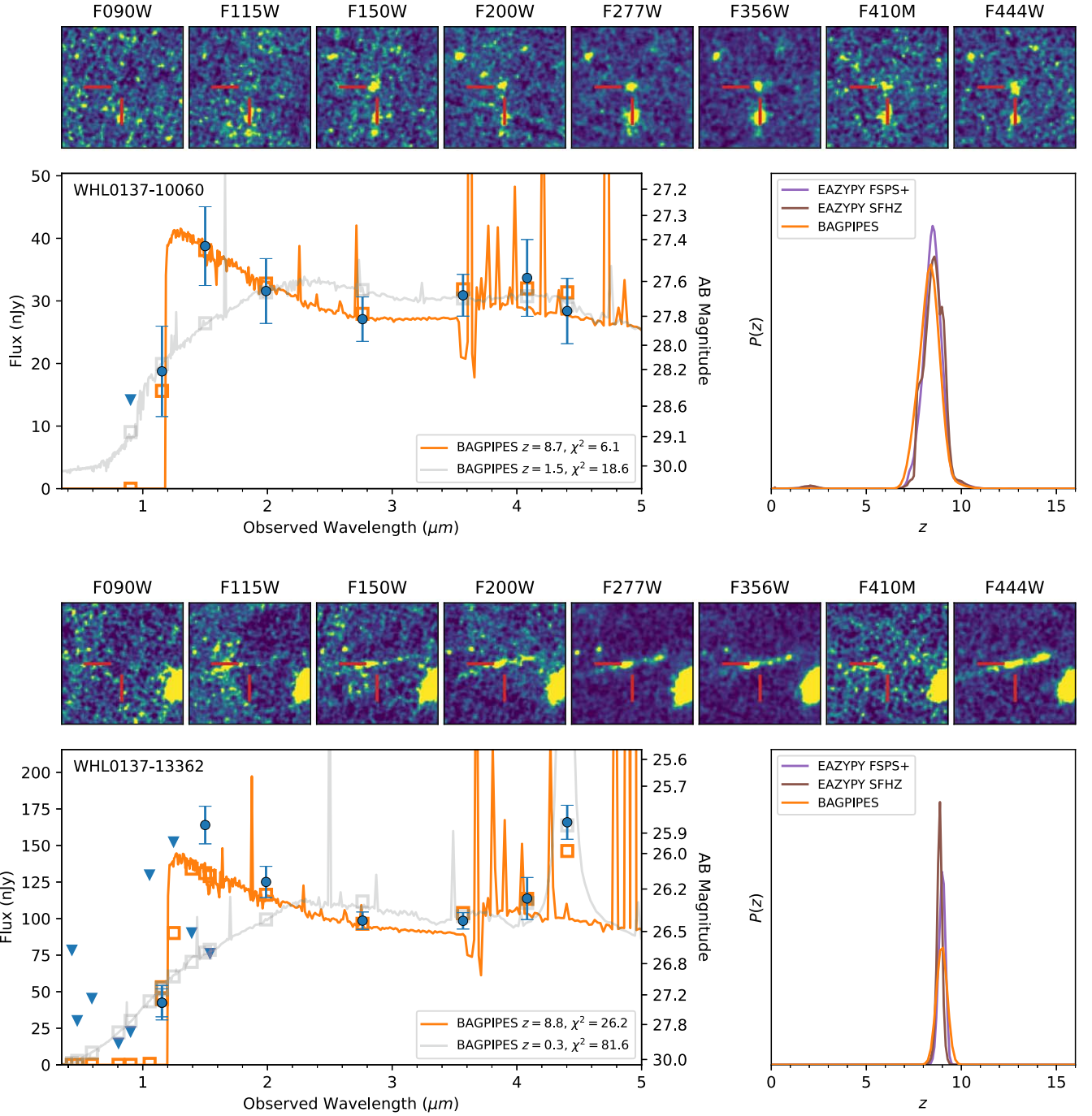


Figure 4. Same as Figure 3, but for the high-redshift galaxy candidates WHL0137-ID10060 and WHL0137-ID13362.

We also emphasize that, given the large magnification uncertainties for WHL0137-ID13362, due to the lack of a multiply imaged sources in the WHL0137-08 cluster, the intrinsic stellar mass and SFR of this galaxy are highly uncertain. As a result, in addition to the SED fitting uncertainties shown in Tables 4 and 5, the derived stellar mass and SFR can vary systematically by factors of 0.75 – 1.5.

4.6. A Gravitationally Lensed Arc at $z \sim 9$

The lensed high-redshift candidate, WHL0137-ID13362, is stretched into an arc $2''.4$ long by the effects of strong gravitational lensing. The arc has at least two bright knots of unevenly distributed star formation (see Figure 5). This

candidate has a lensed F200W AB magnitude of 26.2 ± 0.1 . Assuming a magnification of $\mu = 7.9$ ($\mu = 2.4\text{--}20.2$; see Section 4.2), its intrinsic F200W AB magnitude is 28.4 ± 0.1 .

The BAGPIPES and BEAGLE SED fitting results for WHL0137-ID13362 yield a photometric redshift of $z = 9.0^{+0.2}_{-0.3}$. The redshift posterior distribution $P(z)$ (see Figure 4) for all SED fitting codes, including EAZY, shows a very narrow distribution peaked at $z \sim 9$.

Additional NIRSpect multiobject spectroscopy observations using the microshutter assembly were obtained in December 2022 (GO 2282: PI Coe). While these observations were obtained primarily to study Earendel and the Sunrise Arc in more detail, we were also able to put a slitlet on the $z \sim 9$ arc

Table 4
BAGPIPES Photometric Redshifts and Physical Properties of the High-redshift Galaxy Candidates

Object ID	μ_{mean}^a	z_{phot}^b	z_{phot}^c $z > 7$	$\log M_*/M_\odot$	SFR^d $M_\odot \text{ yr}^{-1}$	$\log \text{sSFR}/\text{Gyr}^{-1}$	Age ^e Myr	A_V mag	t_{form}^f Myr
WHL0137-08004	...	$8.7^{+0.1}_{-0.3}$	$8.8^{+0.1}_{-1.0}$	$8.39^{+0.04}_{-0.07}$	$2.5^{+0.3}_{-0.4}$	$1.0^{+0.0}_{-0.0}$	2^{+1}_{-1}	$0.15^{+0.02}_{-0.02}$	556
WHL0137-09319	...	$9.9^{+1.1}_{-0.8}$	$9.9^{+1.2}_{-0.8}$	$8.74^{+0.18}_{-0.27}$	$4.5^{+1.4}_{-1.3}$	$0.9^{+0.1}_{-0.2}$	79^{+51}_{-49}	$0.09^{+0.06}_{-0.05}$	392
WHL0137-10060	...	$8.4^{+1.0}_{-1.2}$	$8.3^{+0.9}_{-1.0}$	$8.43^{+0.19}_{-0.24}$	$2.3^{+0.4}_{-0.5}$	$1.0^{+0.1}_{-0.2}$	73^{+67}_{-42}	$0.04^{+0.04}_{-0.03}$	518
WHL0137-13362	8^{+12}_{-6}	$9.0^{+0.2}_{-0.3}$	$9.0^{+0.3}_{-0.3}$	$8.31^{+0.08}_{-0.17}$	$1.2^{+0.1}_{-0.1}$	$0.8^{+0.2}_{-0.1}$	132^{+37}_{-56}	$0.02^{+0.02}_{-0.01}$	406

Notes. Physical parameter results are quoted for high-redshift solutions restricting $z > 7$. We quote the median and the 1σ range of the joint posterior distributions for each galaxy. We have modeled star formation histories using an exponential delayed τ model. If constant star formation histories are assumed, age estimates decrease and sSFR increases. For the lensed source, stellar masses and SFRs are corrected for the mean magnification. Multiply these values by μ_{mean}/μ to apply a different magnification. We did not propagate magnification uncertainties to those parameter uncertainties.

^a Mean magnification and uncertainties based on multiple independent lens models. Candidates in the nearby field are estimated to have magnifications of $\mu \leq 1.1$.

^b Photometric redshift with 2σ uncertainties, using the Calzetti dust law (Calzetti et al. 2000).

^c Photometric redshift restricted to $z > 7$ with 2σ uncertainties, using the SMC dust law (Salim et al. 2018).

^d Star formation rate during the past 100 Myr.

^e Mass-weighted age for the delayed τ star formation history.

^f Formation time in Myr after the Big Bang based on the mass-weighted age.

WHL0137-ID13362. The NIRSpec prism spectroscopy covers $0.6\text{--}5.3 \mu\text{m}$ with $R \sim 30\text{--}300$ with 3720 s of exposure time. The NIRSpec data reveal H β and [O III] $\lambda\lambda 4959, 5007$ emission lines at $z = 8.22$, confirming this high-redshift galaxy (Vikaeus et al. in prep).

After correcting for magnification, the BAGPIPES results yield a stellar mass of $\log M_*/M_\odot = 8.31^{+0.08}_{-0.17}$ and a star formation rate of $1.2^{+0.1}_{-0.1} M_\odot \text{ yr}^{-1}$. The galaxy is relatively young, with a mass-weighted age of 132^{+37}_{-56} Myr and a formation redshift of $z_{\text{form}} = 11.1$ ($t_{\text{form}} = 406$ Myr). The BEAGLE results yield a nearly identical stellar mass of $\log M_*/M_\odot = 8.30^{+0.12}_{-0.13}$ and a lower star formation rate of $0.4^{+3.0}_{-0.4} M_\odot \text{ yr}^{-1}$. BEAGLE gives an even younger mass-weighted age of 34^{+15}_{-10} Myr and a formation redshift of $z_{\text{form}} = 9.4$ ($t_{\text{form}} = 504$ Myr).

With a photometric redshift of $z_{\text{phot}} \sim 9$ ($z_{\text{spec}} = 8.22$), WHL0137-ID13362 is the most spatially resolved galaxy at this redshift known to date. Only SPT0615-JD1, the gravitationally lensed $2''.5$ long arc, is more distant at $z \sim 10$ (Salmon et al. 2018). We show an $8''.5 \times 5''.5$ cutout image of WHL0137-ID13362 from the JWST detection image in Figure 5. Assuming a primarily linear and tangential magnification of $\mu \sim 8$, the intrinsic size of the arc is 1.4 kpc at $z = 8.22$. Given the F150W point-spread function full width at half maximum of $\sim 0''.05$ ($\sim 237 \text{ pc}$ at $z = 8.22$), we can resolve $\sim 30 \text{ pc}$ scales in this $z = 8.22$ galaxy.

Unfortunately, WHL0137-08 has no multiple-image constraints in the northeast section of the cluster, where we find this $z \sim 9$ arc. This adds considerable uncertainty to predictions of counterimage locations. While some models (Lenstool) predict two merging images of the arc, and a third image near the cluster center, other models (LTM) predict no counterimages. Although it is not the case with the current lens models, it is possible that the two knots in the arc could be multiple images if the critical curve happens to pass through the arc. Despite the lensing uncertainties, we have identified a promising counterimage (WHL0137-ID06156) $4''$ to the west of the arc (R.A. = 24.3539132° , decl. = -8.44778165° , J2000) with a similar color. While this source is 1.8 mag fainter than the $z \sim 9$ arc, EAZY estimates its $z_{\text{phot}} = 8.2^{+0.6}_{-0.4}$, which very closely agrees with the redshift $z_{\text{spec}} = 8.22$ of the main arc. Additional lens modeling is ongoing to further investigate this possibility.

4.7. Number Counts

In this data set, the lensed field yielded one candidate, fewer than the three identified in the nearby blank field. While this difference may simply be due to small-number statistics, we explore other possible reasons.

As discussed in Section 4.2, lensing reduces the area of the source plane at high redshifts. Using our cluster lens models, we estimate the ratio of the source-plane area at $z = 9$ of the lensed cluster field to the nearby parallel field ranges from 0.24 to 0.85. Because of a lack of multiply imaged sources, the lens models have large uncertainties, yielding a factor of 3.5 difference in the source-plane area at high redshift.

Furthermore, there are more bright foreground galaxies in the cluster field than the blank field. The galaxy cluster can also hamper detections somewhat, though advanced methods can model and/or filter out the brighter cluster light to recover many faint distant galaxies (e.g., Livermore et al. 2017; Bhatawdekar & Conselice 2021). Using the regions of segmentation image without source detections, we find that the blank area of the cluster field is 9% smaller than the parallel field (3.9 versus 4.3 arcmin^2). Taken together, the high-redshift source-plane area in the cluster field may be $\sim 0.21\text{--}0.77$ times smaller than the parallel field. Assuming a similar surface number density of high-redshift sources over the two fields (although this is not necessarily the case, due to cosmic variance), we would expect a reduction in the number of high-redshift sources in the lensed field by the same factors.

Our results identify one high-redshift candidate in the cluster field, WHL0137-ID13362, which with a delensed magnitude of 28.4 (F200W) would have been detected without lensing. Thus, our number count ratio between the two fields of 0.33 is consistent with the range of 0.21–0.77. However, this does not consider the effect of lensing magnification bias (e.g., Broadhurst et al. 1995). In a flux-limited sample, the lensed field, due to the magnification effect, probes galaxies from a fainter source population than the unlensed field.

At $z \sim 8$, faint number counts in lensed fields should roughly match those in blank fields (e.g., Coe et al. 2015), given the observed steep faint-end slope $\alpha \sim -2$ of the UV luminosity function (LF) (e.g., Bradley et al. 2012; Bouwens et al. 2022). At higher redshifts $z \gtrsim 9$, we expect steeper LF faint-end slopes, increasing the advantage for lensing to reveal faint

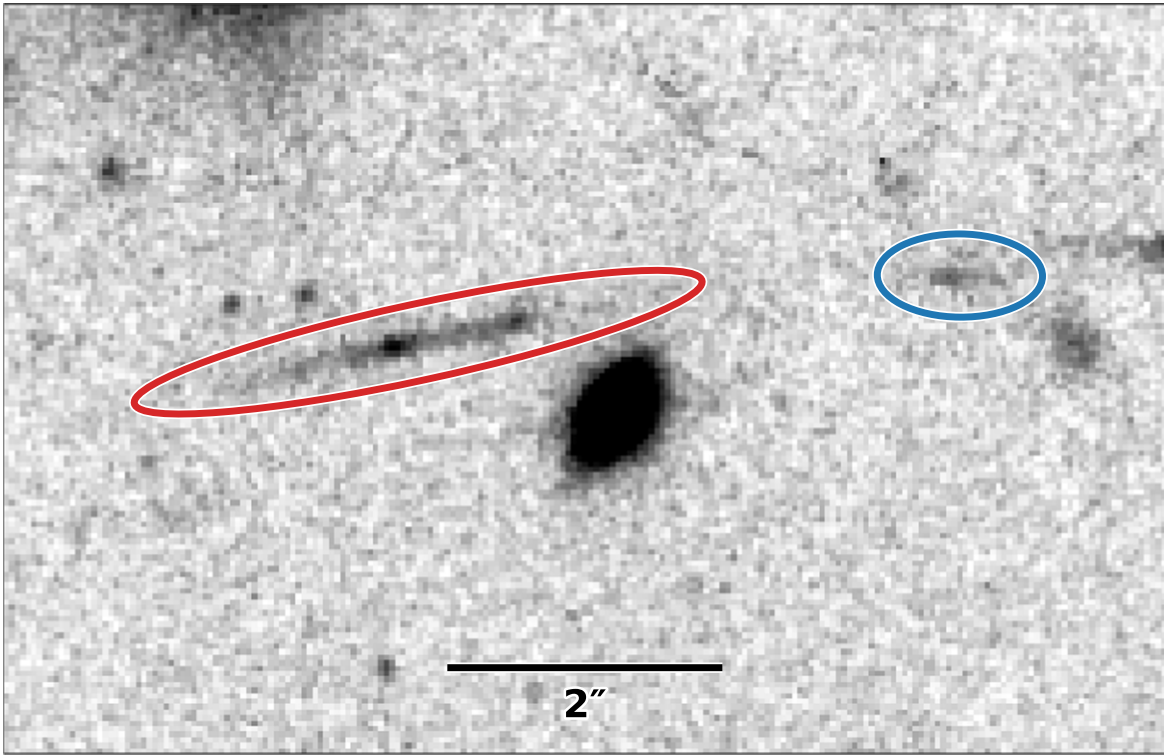


Figure 5. An $8''.5 \times 5''.5$ cutout image from the JWST NIRCam detection image showing the $z \sim 9$ arc WHL0137-ID13362 (red outline), with a magnification of $\mu \sim 8$. The arc is $2''.4$ long, has at least two bright star-forming knots, and is the most spatially resolved arc at $z \sim 9$ known to date. A potential fainter counterimage of the arc, with a similar color and photometric redshift, is also shown outlined in blue.

Table 5
BEAGLE Photometric Redshifts and Physical Properties of the High-redshift Galaxy Candidates

Object ID	μ_{mean}^a	z_{phot}	$\log M_*/M_\odot$	SFR $M_\odot \text{ yr}^{-1}$	$\log \text{sSFR/Gyr}$	Age ^b Myr	A_V mag	β^c	M_{UV}^d
WHL0137-08004	...	$10.2^{+0.1}_{-0.1}$	$10.19^{+0.05}_{-0.04}$	$0.1^{+0.4}_{-0.1}$	$-2.2^{+0.7}_{-0.7}$	236^{+44}_{-46}	$0.02^{+0.02}_{-0.01}$	-1.5 ± 0.1	-22.4
WHL0137-09319	...	$10.1^{+0.5}_{-0.5}$	$8.66^{+0.31}_{-0.50}$	$5.4^{+2.5}_{-5.1}$	$1.0^{+0.7}_{-1.5}$	33^{+73}_{-19}	$0.11^{+0.09}_{-0.06}$	-2.0 ± 0.2	-19.8
WHL0137-10060	...	$8.3^{+0.6}_{-0.6}$	$8.37^{+0.10}_{-0.17}$	$0.3^{+1.4}_{-0.3}$	$0.1^{+0.9}_{-1.0}$	17^{+10}_{-4}	$0.09^{+0.08}_{-0.06}$	-2.2 ± 0.2	-19.0
WHL0137-13362	8^{+12}_{-6}	$9.0^{+0.2}_{-0.2}$	$8.30^{+0.12}_{-0.13}$	$0.4^{+3.0}_{-0.4}$	$-0.6^{+1.1}_{-1.2}$	34^{+15}_{-10}	$0.02^{+0.03}_{-0.01}$	-2.6 ± 0.1	-18.7

Notes. Results are quoted as the median and the 1σ range of the joint posterior distributions for each galaxy. For the lensed source, stellar masses and SFRs are corrected for magnification. Multiply these values by μ_{mean}/μ to apply a different magnification. We did not propagate magnification uncertainties to those parameter uncertainties.

^a Mean magnification and uncertainties based on multiple independent lens models. Candidates in the nearby field are estimated to have magnifications of $\mu \leq 1.1$.

^b Mass-weighted age in Myr.

^c Rest-frame UV slope.

^d Rest-frame absolute UV magnitude in the band that contains 1500 \AA at the galaxy's photometric redshift.

galaxies at these redshifts. More detailed analyses injecting artificial sources and measuring completeness will be required of this and other fields, to quantify the lensing advantage at $z \sim 9$ and higher redshifts. Confirmed suppression of lensed number counts could indicate LF faint-end slopes hovering around $\alpha \sim -2$ rather than steepening as expected from both simulations and trends at lower redshifts. However, we can draw no conclusions, given the very small samples sizes presented in this paper.

4.8. Possible Sources of Contamination

Low-mass stars, extreme emission-line galaxies (EELG), and photometric scatter of red low-redshift galaxies can all be sources of contamination for high-redshift galaxy selections. While low-mass stars and brown dwarfs can have colors similar

to those of high-redshift galaxies (e.g., Yan et al. 2003; Ryan et al. 2005; Wilkins et al. 2014), we can rule out the possibility of contamination from these sources because all of our candidates are resolved (see Section 4.3). Galaxies with extremely strong emission lines can sometimes also mimic high-redshift galaxies, especially in cases with fewer filters longward of the spectral break (Atek et al. 2011; van der Wel et al. 2011; Brammer et al. 2013). With our multiband data set, we have six filters redward of the break, and our SED models are flexible to include extreme emission lines (as in the case of our BEAGLE fit to WHL0137-ID8004, which implies $[\text{O III}] + \text{H}\beta$ rest-frame equivalent width $\sim 2000 \text{ \AA}$).

Low-redshift red and dust-obscured galaxies can also be a source of contamination, where their strong Balmer breaks can be confused with a $\text{Ly}\alpha$ break. Using HST data,

Bouwens et al. (2011) found that the contamination rates of low-redshift interlopers can be up to 40%. However, this can be somewhat mitigated by having many filters redward of the break. Red or dusty low-redshift interlopers are expected to have red colors longward of break, which is not the case for three of our candidates. Three of our candidates have very blue SED longward of the break, with continuum slopes of $\beta < -2$. The remaining candidate, WHL0137-ID8004, has a redder continuum slope of $\beta = -1.5$. The SED fitting results differ significantly, fitting the redder continuum with either very strong emission lines or a Balmer break, leading to completely different interpretations for this galaxy. However, SED fits constrained to low redshifts ($z < 7$) provide much poorer solutions for this galaxy.

As part of our sample selection, we ran addition SED fits in which we forced the photometric redshifts to $z < 7$ in order to determine if the breaks (and fluxes in all bands) can be fit well by a low-redshift solution. Our selection criteria require a conservative χ^2 difference of at least 9 between the low-redshift and high-redshift solutions, indicating much poorer fits for the low-redshift solutions and ruling them out at $\geq 3\sigma$ significance (Harikane et al. 2023).

We also consider the possibility that we may have detected more high-redshift candidates in the parallel field because it lacks HST coverage in bluer filters, which might have helped rule out low-redshift interlopers. To explore this possibility, we reran EAZY on the sources in the lensed field using only their fluxes in the JWST NIRCcam filters, excluding the photometry in all HST filters. After performing the same selection criteria as for the parallel field, we find only one additional high-redshift candidate. This would suggest that our contamination rate is not significantly affected due to the lack of HST photometry in the parallel field. Formally, inclusion of the HST data excludes 50% of our candidates in the lensed field, but this represents only one galaxy. Strong conclusions cannot be drawn from this small sample size.

While our high-redshift sample selection criteria are designed to minimize contamination from low-redshift interlopers, the possibility remains that some of our candidates are at lower redshifts. Spectroscopic confirmation, like that obtained for WHL0137-ID13362, is needed in order to definitively measure the redshifts of these candidates.

5. Conclusions

We present a search for very high-redshift galaxies in the first JWST NIRCcam observations of the lensing cluster WHL0137-08 and a nearby parallel field centered $\sim 2.9'$ from the cluster center. Combined with RELICS HST observations, the JWST and HST observations of WHL0137-08 include imaging in 17 filters spanning $0.4\text{--}5.0\ \mu\text{m}$ that we use to search for high-redshift galaxies.

Our final sample of high-redshift candidate galaxies consists of four candidates with photometric redshifts $z_{\text{phot}} \sim 8.3\text{--}10.2$. We note that, while our initial EAZY selection was restricted to $z_{\text{phot}} \geq 8.5$, the BAGPIPES and BEAGLE photometric redshift for one of the candidates (WHL0137-ID10060) is at $z_{\text{phot}} = 8.3\text{--}8.4$. One $z_{\text{phot}} \sim 9$ candidate, WHL0137-ID13362, lies in the cluster field, while the remaining three are located in the nearby parallel field.

One candidate, WHL0137-ID13362, is magnified to AB mag 26.2 and stretched into an arc $2.4''$ long by the effects of strong gravitational lensing. The JWST data reveal at least two

bright knots of unevenly distributed star formation within the arc. This candidate also has a magnification $\mu = 7.9^{+12}_{-6}$ as determined from four independent lens models of the WHL0137-08 galaxy cluster. WHL0137-ID13362 is the most spatially resolved galaxy at $z_{\text{phot}} \sim 9$ known to date, similar in length to the $z_{\text{phot}} \sim 10$ candidate SPT0615-JD1 (Salmon et al. 2018). Recent JWST NIRSpec observations spectroscopically confirm this galaxy at $z_{\text{spec}} = 8.22$ (Vikaeus et al., in prep).

We perform SED fitting to the photometry of these galaxies using the independent SED-fitting codes BAGPIPES and BEAGLE to estimate the physical properties of our candidates. We find stellar masses typically in the range $\log M_*/M_\odot = 8.3\text{--}8.7$, specific star formation rates $\text{sSFR} \sim 0.25\text{--}10\ \text{Gyr}^{-1}$, young mass-weighted ages $< 240\ \text{Myr}$, low dust content with values $A_V < 0.15$, and rest-frame UV slopes of $\beta = -1.5$ to -2.6 . We note that the stellar masses and SFR of the lensed galaxy WHL0137-ID13362 are highly uncertain because of magnification uncertainties.

Other JWST analyses have estimated similarly young ages $< 100\ \text{Myr}$ for $z \sim 9\text{--}16$ candidates (Furtak et al. 2023; Whittler et al. 2023). Discovering such young galaxies is consistent with expectations from simulations, given our image depths down to AB mag ~ 29 (Mason et al. 2023). Deeper JWST imaging is required in order to reveal older (and thus fainter) $\sim 100\ \text{Myr}$ populations at $z > 9$, perhaps typical for the more numerous fainter galaxies in the early Universe. Likewise, JWST/NIRSpec observations will be needed in order to spectroscopically confirm three of these high-redshift galaxy candidates and to study their physical properties in more detail.













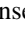







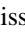





Acknowledgments

Based on observations with the NASA/ESA/CSA James Webb Space Telescope obtained from the Mikulski Archive for Space Telescopes (MAST) at the Space Telescope Science Institute (STScI), which is operated by the Association of Universities for Research in Astronomy (AURA), Incorporated, under NASA contract NAS5-03127. Support for Program number JWST-GO-02282 was provided through a grant from the STScI under NASA contract NAS5-03127. The data described here may be obtained from the MAST archive at doi:10.17909/cqfq-5n80. Also based on observations made with the NASA/ESA Hubble Space Telescope, obtained at STScI, which is operated by AURA under NASA contract NAS5-26555. The HST observations are associated with programs HST-GO-14096, HST-GO-15842, and HST-GO-16668. Cloud-based data processing and file storage for this work is provided by the AWS Cloud Credits for Research program. The Cosmic Dawn Center is funded by the Danish National Research Foundation (DNRF) under grant #140. A.Z. and L.F. acknowledge support by grant No. 2020750 from the United States-Israel Binational Science Foundation (BSF) and grant No. 2109066 from the United States National Science Foundation (NSF), and by the Ministry of Science & Technology, Israel.

Facilities: JWST(NIRCcam), HST(ACS, WFC3).

Software: ASTROPY (Astropy Collaboration et al. 2018, 2022), PHOTUTILS (Bradley 2023), GRIZLI (Brammer et al. 2022), EAZY (Brammer et al. 2008), BAGPIPES (Carnall et al. 2018), BEAGLE (Chevallard & Charlot 2016), JDAVIZ (JDADF Developers et al. 2022).

ORCID iDs

Larry D. Bradley  <https://orcid.org/0000-0002-7908-9284>
 Dan Coe  <https://orcid.org/0000-0001-7410-7669>
 Gabriel Brammer  <https://orcid.org/0000-0003-2680-005X>
 Lukas J. Furtak  <https://orcid.org/0000-0001-6278-032X>
 Rebecca L. Larson  <https://orcid.org/0000-0003-2366-8858>
 Vasily Kokorev  <https://orcid.org/0000-0002-5588-9156>
 Felipe Andrade-Santos  <https://orcid.org/0000-0002-8144-9285>
 Rachana Bhatawdekar  <https://orcid.org/0000-0003-0883-2226>
 Maruša Bradač  <https://orcid.org/0000-0001-5984-0395>
 Tom Broadhurst  <https://orcid.org/0000-0002-8785-8979>
 Adam Carnall  <https://orcid.org/0000-0002-1482-5818>
 Christopher J. Conselice  <https://orcid.org/0000-0003-1949-7638>
 Jose M. Diego  <https://orcid.org/0000-0001-9065-3926>
 Brenda Frye  <https://orcid.org/0000-0003-1625-8009>
 Seiji Fujimoto  <https://orcid.org/0000-0001-7201-5066>
 Tiger Y.-Y. Hsiao  <https://orcid.org/0000-0003-4512-8705>
 Taylor A. Hutchison  <https://orcid.org/0000-0001-6251-4988>
 Intae Jung  <https://orcid.org/0000-0003-1187-4240>
 Guillaume Mahler  <https://orcid.org/0000-0003-3266-2001>
 Stephan McCandliss  <https://orcid.org/0000-0003-0503-4667>
 Masamune Oguri  <https://orcid.org/0000-0003-3484-399X>
 Marc Postman  <https://orcid.org/0000-0002-9365-7989>
 Keren Sharon  <https://orcid.org/0000-0002-7559-0864>
 M. Trenti  <https://orcid.org/0000-0001-9391-305X>
 Eros Vanzella  <https://orcid.org/0000-0002-5057-135X>
 Brian Welch  <https://orcid.org/0000-0003-1815-0114>
 Rogier A. Windhorst  <https://orcid.org/0000-0001-8156-6281>
 Adi Zitrin  <https://orcid.org/0000-0002-0350-4488>

References

- Adams, N. J., Conselice, C. J., Ferreira, L., et al. 2023, *MNRAS*, **518**, 4755
 Aihara, H., Allende Prieto, C., An, D., et al. 2011, *ApJS*, **193**, 29
 Astropy Collaboration, Price-Whelan, A. M., Lim, P. L., et al. 2022, *ApJ*, **935**, 167
 Astropy Collaboration, Price-Whelan, A. M., Sipőcz, B. M., et al. 2018, *AJ*, **156**, 123
 Atek, H., Richard, J., Jauzac, M., et al. 2015, *ApJ*, **814**, 69
 Atek, H., Richard, J., Kneib, J. P., & Schaerer, D. 2018, *MNRAS*, **479**, 5184
 Atek, H., Shuntov, M., Furtak, L. J., et al. 2023, *MNRAS*, **519**, 1201
 Atek, H., Siana, B., Scarlata, C., et al. 2011, *ApJ*, **743**, 121
 Bhatawdekar, R., & Conselice, C. J. 2021, *ApJ*, **909**, 144
 Bhatawdekar, R., Conselice, C. J., Margalef-Bentabol, B., & Duncan, K. 2019, *MNRAS*, **486**, 3805
 Bouwens, R., Illingworth, G., Oesch, P., et al. 2023, *MNRAS*, **523**, 1009
 Bouwens, R. J., Bradley, L., Zitrin, A., et al. 2014, *ApJ*, **795**, 126
 Bouwens, R. J., Illingworth, G., Ellis, R. S., et al. 2022, *ApJ*, **931**, 81
 Bouwens, R. J., Illingworth, G. D., Oesch, P. A., et al. 2011, *ApJ*, **737**, 90
 Bouwens, R. J., Oesch, P. A., Illingworth, G. D., Ellis, R. S., & Stefanon, M. 2017, *ApJ*, **843**, 129
 Boylan-Kolchin, M. 2023, *NatAs*, **7**, 731
 Bradley, L. 2023, *astropy/photutils*: 1.8.0, 1.8.0, Zenodo, doi:10.5281/zenodo.7946442
 Bradley, L. D., Bouwens, R. J., Ford, H. C., et al. 2008, *ApJ*, **678**, 647
 Bradley, L. D., Trenti, M., Oesch, P. A., et al. 2012, *ApJ*, **760**, 108
 Bradley, L. D., Zitrin, A., Coe, D., et al. 2014, *ApJ*, **792**, 76
 Brammer, G., Strait, V., Matharu, J., & Momcheva, I. 2022, *grizli* (1.5.0), Zenodo, doi:10.5281/zenodo.6672538
 Brammer, G. B., van Dokkum, P. G., & Coppi, P. 2008, *ApJ*, **686**, 1503
 Brammer, G. B., van Dokkum, P. G., Illingworth, G. D., et al. 2013, *ApJL*, **765**, L2
 Broadhurst, T., Benítez, N., Coe, D., et al. 2005, *ApJ*, **621**, 53
 Broadhurst, T. J., Taylor, A. N., & Peacock, J. A. 1995, *ApJ*, **438**, 49
 Bruzual, G., & Charlot, S. 2003, *MNRAS*, **344**, 1000
 Calzetti, D., Armus, L., Bohlin, R. C., et al. 2000, *ApJ*, **533**, 682
 Capak, P. L., Carilli, C., Jones, G., et al. 2015, *Natur*, **522**, 455
 Carnall, A. C., Begley, R., McLeod, D. J., et al. 2023, *MNRAS*, **518**, L45
 Carnall, A. C., McLure, R. J., Dunlop, J. S., & Davé, R. 2018, *MNRAS*, **480**, 4379
 Castellano, M., Fontana, A., Treu, T., et al. 2022, *ApJL*, **938**, L15
 Chabrier, G. 2003, *PASP*, **115**, 763
 Chevallard, J., & Charlot, S. 2016, *MNRAS*, **462**, 1415
 Coe, D., Bradley, L., & Zitrin, A. 2015, *ApJ*, **800**, 84
 Coe, D., Salmon, B., Bradač, M., et al. 2019, *ApJ*, **884**, 85
 Coe, D., Zitrin, A., Carrasco, M., et al. 2013, *ApJ*, **762**, 32
 Conroy, C., & Gunn, J. E. 2010, *ApJ*, **712**, 833
 Conroy, C., Gunn, J. E., & White, M. 2009, *ApJ*, **699**, 486
 Conroy, C., White, M., & Gunn, J. E. 2010, *ApJ*, **708**, 58
 Diego, J. M., Protopapas, P., Sandvik, H. B., & Tegmark, M. 2005, *MNRAS*, **360**, 477
 Diego, J. M., Tegmark, M., Protopapas, P., & Sandvik, H. B. 2007, *MNRAS*, **375**, 958
 Donnan, C. T., McLeod, D. J., Dunlop, J. S., et al. 2023, *MNRAS*, **518**, 6011
 Endsley, R., Stark, D. P., Whitler, L., et al. 2023, *MNRAS*, **524**, 2312
 Ferland, G. J., Porter, R. L., van Hoof, P. A. M., et al. 2013, *RMxAA*, **49**, 137
 Feroz, F., & Hobson, M. P. 2008, *MNRAS*, **384**, 449
 Feroz, F., Hobson, M. P., & Bridges, M. 2009, *MNRAS*, **398**, 1601
 Feroz, F., & Skilling, J. 2013, in *AIP Conf. Ser.* 1553, *Bayesian Inference and Maximum Entropy Methods in Science and Engineering: 32nd Int. Workshop on Bayesian Inference and Maximum Entropy Methods in Science and Engineering*, ed. U. von Toussaint (Melville, NY: AIP), 106
 Ferrara, A., Pallottini, A., & Dayal, P. 2023, *MNRAS*, **522**, 3986
 Finkelstein, S. L., Bagley, M. B., Arrabal Haro, P., et al. 2022, *ApJL*, **940**, L55
 Finkelstein, S. L., Bagley, M. B., Ferguson, H. C., et al. 2023, *ApJL*, **946**, L13
 Frye, B., & Broadhurst, T. 1998, *ApJL*, **499**, L115
 Frye, B. L., Bowen, D. V., Hurley, M., et al. 2008, *ApJL*, **685**, L5
 Furtak, L. J., Atek, H., Lehnert, M. D., Chevallard, J., & Charlot, S. 2021, *MNRAS*, **501**, 1568
 Furtak, L. J., Shuntov, M., Atek, H., et al. 2023, *MNRAS*, **519**, 3064
 Gaia Collaboration, Brown, A. G. A., & Vallenari, A. 2021, *A&A*, **649**, A1
 Gutkin, J., Charlot, S., & Bruzual, G. 2016, *MNRAS*, **462**, 1757
 Harikane, Y., Ouchi, M., Oguri, M., et al. 2023, *ApJS*, **265**, 5
 Hoag, A., Bradač, M., Trenti, M., et al. 2017, *NatAs*, **1**, 0091
 Hoffmann, S. L., Mack, J., Avila, R., et al. 2021, *AAS Meeting*, **53**, 216.02
 Infante, L., Zheng, W., Laporte, N., et al. 2015, *ApJ*, **815**, 18
 Inoue, A. K., Shimizu, I., Iwata, I., & Tanaka, M. 2014, *MNRAS*, **442**, 1805
 Ishigaki, M., Kawamata, R., Ouchi, M., et al. 2015, *ApJ*, **799**, 12
 JDADF Developers, Averbukh, J., & Bradley, L. 2022, *Jdaviz*, doi:10.5281/zenodo.5513927
 Jullo, E., & Kneib, J. P. 2009, *MNRAS*, **395**, 1319
 Jullo, E., Kneib, J. P., Limousin, M., et al. 2007, *NJPh*, **9**, 447
 Koekemoer, A. M., Fruchter, A. S., Hook, R. N., & Hack, W. 2003, in *HST Calibration Workshop: Hubble after the Installation of the ACS and the NICMOS Cooling System*, ed. S. Santiago, A. Koekemoer, & B. Whitmore (Baltimore, MD: Space Telescope Science Institute), 337
 Kokorev, V., Brammer, G., Fujimoto, S., et al. 2022, *ApJS*, **263**, 38
 Kroupa, P. 2002, *Sci*, **295**, 82
 Labbé, I., van Dokkum, P., Nelson, E., et al. 2023, *Natur*, **616**, 266
 Laporte, N., Streblyanska, A., Kim, S., et al. 2015, *A&A*, **575**, A92
 Larson, R. L., Hutchison, T. A., Bagley, M., et al. 2022, *arXiv:2211.10035*
 Leethochawalit, N., Trenti, M., Santini, P., et al. 2023, *ApJL*, **942**, L26
 Livermore, R. C., Finkelstein, S. L., & Lotz, J. M. 2017, *ApJ*, **835**, 113
 Lotz, J. M., Koekemoer, A., Coe, D., et al. 2017, *ApJ*, **837**, 97
 Lovell, C. C., Harrison, I., Harikane, Y., Tacchella, S., & Wilkins, S. M. 2023, *MNRAS*, **518**, 2511
 Mason, C. A., Trenti, M., & Treu, T. 2023, *MNRAS*, **521**, 497
 Meštrić, U., Vanzella, E., Zanella, A., et al. 2022, *MNRAS*, **516**, 3532
 Morishita, T., & Stiavelli, M. 2023, *ApJL*, **946**, L35
 Naidu, R. P., Oesch, P. A., van Dokkum, P., et al. 2022a, *ApJL*, **940**, L14
 Naidu, R. P., Oesch, P. A., Setton, D. J., et al. 2022b, *arXiv:2208.02794*
 Naidu, R. P., Oesch, P. A., van Dokkum, P., et al. 2022c, *ApJL*, **940**, L14
 Oesch, P. A., Brammer, G., van Dokkum, P. G., et al. 2016, *ApJ*, **819**, 129
 Oguri, M. 2010, *PASJ*, **62**, 1017
 Oke, J. B. 1974, *ApJS*, **27**, 21
 Oke, J. B., & Gunn, J. E. 1983, *ApJ*, **266**, 713
 Pei, Y. C. 1992, *ApJ*, **395**, 130
 Planck Collaboration, Ade, P. A. R., Aghanim, N., et al. 2016, *A&A*, **594**, A27
 Planck Collaboration, Aghanim, N., Akrami, Y., et al. 2020, *A&A*, **641**, A6

- Pontoppidan, K. M., Barrientes, J., Blome, C., et al. 2022, [ApJL](#), **936**, L14
- Postman, M., Coe, D., Benítez, N., et al. 2012, [ApJS](#), **199**, 25
- Reddy, N. A., Kriek, M., Shapley, A. E., et al. 2015, [ApJ](#), **806**, 259
- Reddy, N. A., Oesch, P. A., Bouwens, R. J., et al. 2018, [ApJ](#), **853**, 56
- Rigby, J., Perrin, M., McElwain, M., et al. 2023, [PASP](#), **135**, 048001
- Ryan, R. E. J., Hathi, N. P., Cohen, S. H., & Windhorst, R. A. 2005, [ApJL](#), **631**, L159
- Salim, S., Boquien, M., & Lee, J. C. 2018, [ApJ](#), **859**, 11
- Salmon, B., Coe, D., Bradley, L., et al. 2018, [ApJL](#), **864**, L22
- Salmon, B., Coe, D., Bradley, L., et al. 2020, [ApJ](#), **889**, 189
- Shivaei, I., Reddy, N., Rieke, G., et al. 2020, [ApJ](#), **899**, 117
- Steinhardt, C. L., Kokorev, V., Rusakov, V., Garcia, E., & Sneppen, A. 2023, [ApJL](#), **951**, L40
- Strait, V., Bradač, M., Coe, D., et al. 2021, [ApJ](#), **910**, 135
- Tacchella, S., Johnson, B. D., Robertson, B. E., et al. 2023, [MNRAS](#), **522**, 6236
- Treu, T., Roberts-Borsani, G., Bradac, M., et al. 2022, [ApJ](#), **935**, 110
- Trussler, J. A. A., Adams, N. J., Conselice, C. J., et al. 2023, [MNRAS](#), **523**, 3423
- Valentino, F., Brammer, G., Gould, K. M. L., et al. 2023, [ApJ](#), **947**, 20
- van der Wel, A., Straughn, A. N., Rix, H. W., et al. 2011, [ApJ](#), **742**, 111
- Vanzella, E., Castellano, M., Bergamini, P., et al. 2022, [A&A](#), **659**, A2
- Welch, B., Coe, D., Zackrisson, E., et al. 2022, [ApJL](#), **940**, L1
- Welch, B., Coe, D., Zitrin, A., et al. 2023, [ApJ](#), **943**, 2
- Wen, Z. L., & Han, J. L. 2015, [ApJ](#), **807**, 178
- Wen, Z. L., Han, J. L., & Liu, F. S. 2012, [ApJS](#), **199**, 34
- Whitler, L., Endsley, R., Stark, D. P., et al. 2023, [MNRAS](#), **519**, 157
- Wilkins, S. M., Stanway, E. R., & Bremer, M. N. 2014, [MNRAS](#), **439**, 1038
- Yan, H., Windhorst, R. A., & Cohen, S. H. 2003, [ApJL](#), **585**, L93
- Yang, L., Morishita, T., Leethochawalit, N., et al. 2022, [ApJL](#), **938**, L17
- Zheng, W., Postman, M., Zitrin, A., et al. 2012, [Natur](#), **489**, 406
- Zitrin, A., Broadhurst, T., Umetsu, K., et al. 2009, [MNRAS](#), **396**, 1985
- Zitrin, A., Fabris, A., Merten, J., et al. 2015, [ApJ](#), **801**, 44
- Zitrin, A., Zheng, W., Broadhurst, T., et al. 2014, [ApJL](#), **793**, L12